From clouds to comets: tracing the molecular journey of interstellar ices in the JWST era

Slavicinska, K.

1 Introduction

1.1 Seeds of life in surprising places

Deep in some of the most remote parts of Earth's oceans along the boundaries of Earth's tectonic plates, hot plumes of liquids and gases bubble through towering mineral chimneys that grow from the bottom of the seafloor. Such *hydrothermal vents* arise when seawater leaks through seafloor cracks and is heated in Earth's mantle, producing fluids rich in reduced gases and dissolved crustal minerals. When these hot fluids are re-expelled into the ocean and meet the near-freezing seawater, the dissolved minerals within them precipitate, resulting in forests of vent chimneys similar in appearance to cave stalagmites (Fig. 1.1).

Given their complete lack of sunlight and the noxious nature of many vent fluid constituents (e.g., H_2S), one may expect hydrothermal vents to be rather desolate in terms of life. Yet despite their seemingly hostile conditions, hydrothermal vents are home to an eclectic collection of benthic creatures: long red tube worms, massive clams, "yeti" crabs with furry claws, eyeless shrimp, pale white octopuses. What's more, these bizarre ecosystems function largely independently of the light-powered world above, fueled primarily by local *chemosynthetic* bacteria and archaea, which harness chemical energy by oxidizing reduced compounds like H_2S to build organic molecules. And while such lifeforms may seem quite alien to us H_2S-averse land-dwellers, there are numerous indications that the last universal common ancestor, from which all currently known life on Earth evolved, was a similar chemosynthetic organism that lived in hot hydrothermal conditions (Pace 1991; Di Giulio 2003; Weiss et al. 2016; Moody et al. 2024). Some origins of life scientists even argue that the abundance of reduced species and catalytic minerals in hydrothermal vents make them prime candidate environments for the origin of life on Earth (Corliss et al. 1981; Russell et al. 1988; Russell & Martin 2004; Martin et al. 2008).

The hydrothermal origin hypothesis is one that remains hotly contested and debated. However, most origins of life researchers and astrobiologists can come to a consensus on one thing: wherever life first formed, there was water. It is the primary molecular constituent of all known life forms; no other molecule comes close to its ability to serve as the ubiquitous solvent of biochemical reactions (Frenkel-Pinter et al. 2021). For this reason, astrobiologists have adopted the motto "follow the water" – initially coined by Mars mission scientists (Hubbard et al. 2002) – to guide the search for extraterrestrial life in the solar system and beyond.

This thesis co-opts this guiding principle, but not in search for extraterrestrial life – rather, in search for the origins of life's most fundamental molecular ingredients. It follows the water

Figure 1.1: Earthly and heavenly pillars of creation. Left: carbonate chimneys in the the Lost City Hydrothermal Field, suggested to be chemically analogous to ancient hydrothermal vents where life may have first formed (Martin et al. 2008). Image credit: D. Kelley/M. Elend/UW/URI-IAO/NOAA/The Lost City Science Team. Right: columnar clouds of interstellar gas and dust in the Serpens star-forming region, as observed by the MIRI instrument onboard the *James Webb* Space Telescope. In the deepest parts of these cloud pillars, copious water and reduced molecules are produced in ice layers on the surfaces of dust grains. Image credit: J. DePasquale/A. Pagan/NASA/ESA/CSA/STScI.

backwards through time in the star and planet formation sequence all the way to its birthplace, another remarkably dark and seemingly desolate place: dense interstellar dust clouds (Fig. 1.1).

The dust in these clouds was expelled into the depths of the interstellar medium by dying stars undergoing mass loss, quite like how organic waste from light-powered ocean life rains down on and fertilizes the ocean's benthic zones. In fact, one could consider this expelled stardust, made of silicates and refractory carbonaceous matter, an effective fertilizer of interstellar chemistry. By blocking radiation and providing catalytic mineral surfaces, this dust creates ideal conditions for forming a plethora of volatile biogenic molecules in ice layers that grow on top of the dust grains.

The most abundant of these molecules is water, which is produced particularly efficiently under these dark and dusty conditions. However, various other species can also be found in these ices, with many of them in reduced form due to the high abundance of hydrogen atoms (e.g., CH_3OH and NH_3), and some of them are quite toxic (e.g., H_2CO and H_2S). Eventually, if the dust cloud gravitationally collapses, causing a star to begin forming at its center, these volatile-enriched dust grains feed the growing star and its surrounding protoplanetary disk, where its planets form. In this way, the ices grown within interstellar dust clouds become one of the primary ingredients of planetary systems and serve as a key source of biogenic volatiles during planet formation.

The work presented in this thesis investigates 1) the chemistry that occurs in interstellar

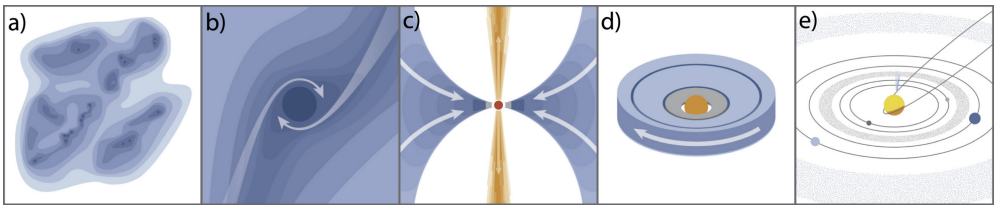

Figure 1.2: Schematic of the star and planetary system formation stages. a) Clouds of dust, ice, and gas with varying densities coalesce in the interstellar medium. b) Gravitational collapse within the densest regions of the clouds triggers star formation. c) A protostar forms and accretes material from its surrounding envelope of cloud material. To conserve angular momentum, the accreted envelope material flattens into a disk shape, and outflows of accreted material are ejected from the source poles. d) The surrounding envelope eventually completely dissipates via accretion or outflows. A protoplanetary disk of accreted material, in which planetesimals form, remains. e) The remaining disk material is either accreted or dissipated, leaving behind a star and its orbiting planetary bodies. Figure from Öberg & Bergin (2021).

ices during these earliest stages of star and planet formation, and 2) how that chemistry sets the stage for the formation of solar systems like our own and the distributions of volatiles within them. To do so, it employs infrared (IR) spectroscopy in a combined experimental and observational approach, where data collected in Earth-based laboratories that simulate interstellar conditions are used to analyze interstellar spectra observed by powerful IR facilities like the *James Webb* Space Telescope (JWST) and its predecessors. The presented studies largely target molecules that have been detected in volatile-rich and primitive small solar system bodies – particularly comets – to assess the chemical link between the interstellar medium and planetary systems. This chapter introduces the reader to the key physical and chemical processes that fundamentally govern interstellar ice chemistry throughout star and planet formation, the techniques used to illuminate these processes, some of the knowledge gaps in the preceding literature, and an overview of how the subsequent chapters of this thesis address them.

1.2 Ice chemistry during star and planet formation

1.2.1 Molecular clouds

The interstellar medium (ISM) – the parts of the universe between stars and their planetary systems – is not just empty space, although its most diffuse regions come very close to it. Here, atomic densities are on the order of $n{\sim}10^2$ cm^{-3}, mainly consisting of hydrogen and some helium atoms formed via fusion shortly after the Big Bang. Additionally, outflows from exploding dying stars supply interstellar space with heavier elements like carbon, nitrogen, oxygen, and sulfur that formed during stellar nucleosynthesis, as well as highly refractory molecules like silicates and polycyclic aromatic hydrocarbons (PAHs) that formed in dense stellar atmospheres and outflows during the end stages of stars' life cycles. Few other molecules can exist in these harsh regions because of extremely high UV and cosmic ray fluxes generated by surrounding stars and supernovae, which destroy all but the strongest chemical bonds.

Some of the refractory materials are expelled from the dying stars in the form of dust

grains with sizes on the order of nm to μm. These grains serve as catalysts, energy sinks, and radiation shields, and they ultimately enable vast networks of chemical reactions to develop in these hostile environments. One of the most important molecules to form on dust grains in the diffuse ISM is H_2 (Hollenbach & Salpeter 1971; Vidali 2013; Wakelam et al. 2017), which would be immediately dissociated by the excess energy released during its formation if formed in the gas phase because H_2 has no allowed rotational or vibrational transitions by which it could release its excess energy of formation. On a grain surface, however, the grain can absorb this energy excess.

The formation of H_2 on grain surfaces kickstarts a gas-phase chemical network by which other molecules (*e.g.*, CO, CH, and CN) form, largely through ion-molecule reactions (Smith 1992). Formation of these molecules competes with their photodissociation via external interstellar radiation. As gravitational instabilities cause the interstellar cloud to grow denser, the external radiation is increasingly shielded from the cloud's interior. The dust within the cloud also scatters light preferentially at shorter wavelengths, leading to the extinction and reddening of incident light. Furthermore, line emission by molecules with dipoles like CO and thermal emission by the dust grains radiatively cools the cloud (Klessen & Glover 2015), increasing the sticking probabilities of atoms and molecules on the dust grain surfaces.

Eventually, temperatures become low enough for the ices studied in this thesis to begin growing on the dust grain surfaces ($\lesssim$20-30 K). These ices form via addition reactions between adsorbed atoms and molecules (Tielens & Hagen 1982). Hydrogen atoms are light and volatile enough to diffuse along the surfaces and hydrogenate larger adsorbed atoms like oxygen, carbon, and nitrogen, leading to the production of reduced species such as H_2O, CH_4, and NH_3 in the form of ices on the grains. The hydrogenation of oxygen into water is particularly efficient; up to $\sim$20% of volatile oxygen atoms within molecular clouds end up locked up in water ice (van Dishoeck et al. 2021). Furthermore, gaseous species can collide with the grains and react with adsorbed atoms and radicals – for example, gaseous CO can react with surface hydroxyl radicals via the HOCO pathway to form CO_2 ice (Oba et al. 2010) and hydrogen atoms to form H_2CO and CH_3OH ice (Hiraoka et al. 1994; Watanabe & Kouchi 2002).

Water ice is observed early at cloud densities on the order of $n\sim10^3$ ($A_v\sim1.5$) (Boogert et al. 2013; Whittet et al. 2013); it is by far the most abundant ice produced at this stage, so this first layer of ices is often referred to as the *polar* ice layer. Other reduced species that form during this stage include CH_4 (Öberg et al. 2008; Qasim et al. 2020) and NH_3 (Hiraoka et al. 1995; Bottinelli et al. 2010). A significant fraction of the NH_3 formed at this stage is converted into NH_4^+ salts via solid-state acid-base reactions, as evidenced by the early appearance of an absorption feature at 6.85 μm (Boogert et al. 2013). The chemical identities of the acids that react with NH_3 to form NH_4^+ salts in the early cloud stage remains a topic of debate; Chapter 4 of this thesis presents an overview of this debate and argues that H_2S is likely the acid responsible for the majority of interstellar NH_4^+ salt formation. Additionally, OH radicals formed on the grains react with CO to produce CO_2 (Whittet et al. 2007; Oba et al. 2010), the second-most abundant observable ice species formed at this stage. Some OH radicals may also react with CH_4 to produce CH_3OH, but in limited quantities compared to later stages (Qasim et al. 2018).

Around $A_v\gtrsim$2-3, CO self-shielding of interstellar radiation becomes extremely efficient, leading to a dramatic increase in gas-phase CO production that further enhances self-shielding in a snowball effect (van Dishoeck & Black 1988; van Dishoeck 1992). Subsequently, as densities continue to increase ($n\gtrsim10^4$, $A_v\gtrsim$3-4), temperatures further drop ($\leq$20 K), enabling the

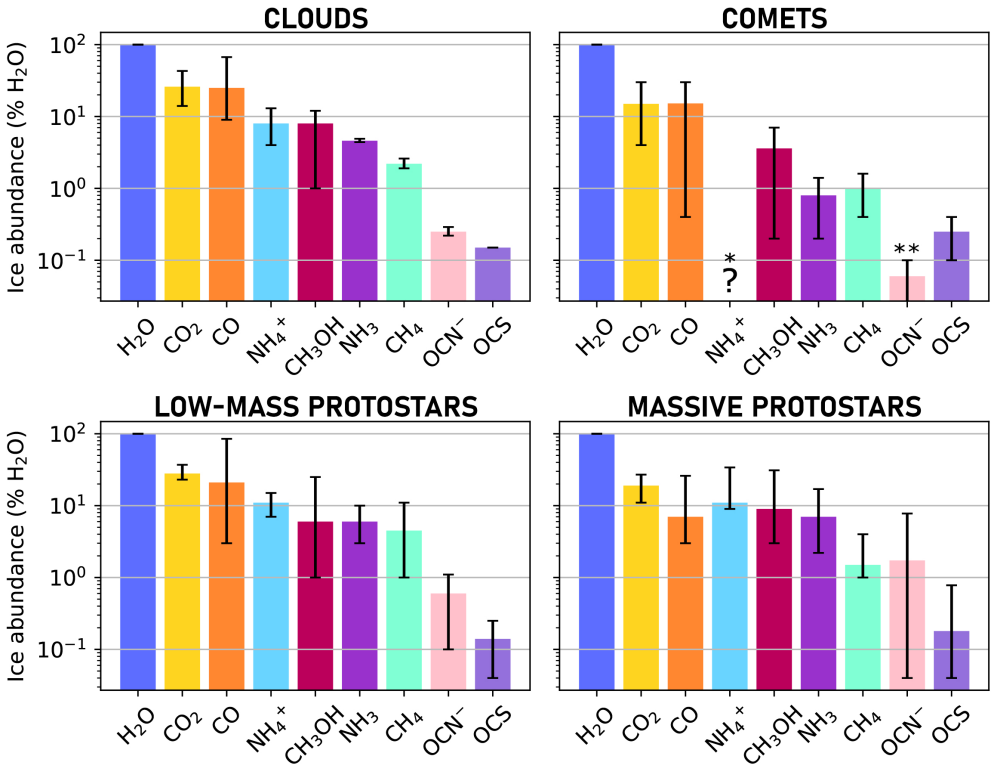

Figure 1.3: Relative ice abundances (with respect to H_2O ice) measured in various stages of star formation and in comets. Cloud values for CO_2, CO, NH_4^+, and CH_3OH are from Boogert et al. (2015); NH_3, CH_4, OCN^-, and OCS values are from McClure et al. (2023). Low-mass protostellar values for all species except OCS are from Boogert et al. (2015); OCS is from in prep work by the author of this thesis. Massive protostellar values for CO_2, CO, NH_4^+, and CH_3OH are from Boogert et al. (2015); NH_3 and CH_4 values are from Gibb et al. (2004); OCN^-, and OCS values are from Boogert et al. (2022). Cometary values for all species except CO_2 are from Mumma & Charnley (2011); CO_2 values are from Ootsubo et al. (2012). *NH_4^+ abundances with respect to water in cometary comae are not known, but presence of NH_4^+ salts in comets has been confirmed with both IR spectroscopy (Poch et al. 2020) and mass spectrometry (Altwegg et al. 2022). **Assumes all HNCO detected in cometary comae is a product of desorbed OCN^- salts.

freeze-out of some of the CO gas on the dust grains. Thus, an *apolar* ice layer begins to grow, dominated by CO, CO_2 produced via CO oxygenation, and likely other more volatile apolar species like N_2 and O_2, although their presence in ices cannot be observationally confirmed due to their IR inactivity (see Section 1.3).

Densities $n \gtrsim 10^5$ ($A_v \gtrsim 9$) mark the beginning of the *catastrophic CO freeze-out* stage, in which conditions are so cold and dense that the vast majority of the cloud CO is frozen out on the grains (Pontoppidan 2006). At these high densities, the hydrogenation of CO ice proceeds rapidly, producing the majority of the CH_3OH ice observed in molecular clouds. For this reason the ice layers grown at these high cloud densities are often referred to as the *CH_3OH-rich*

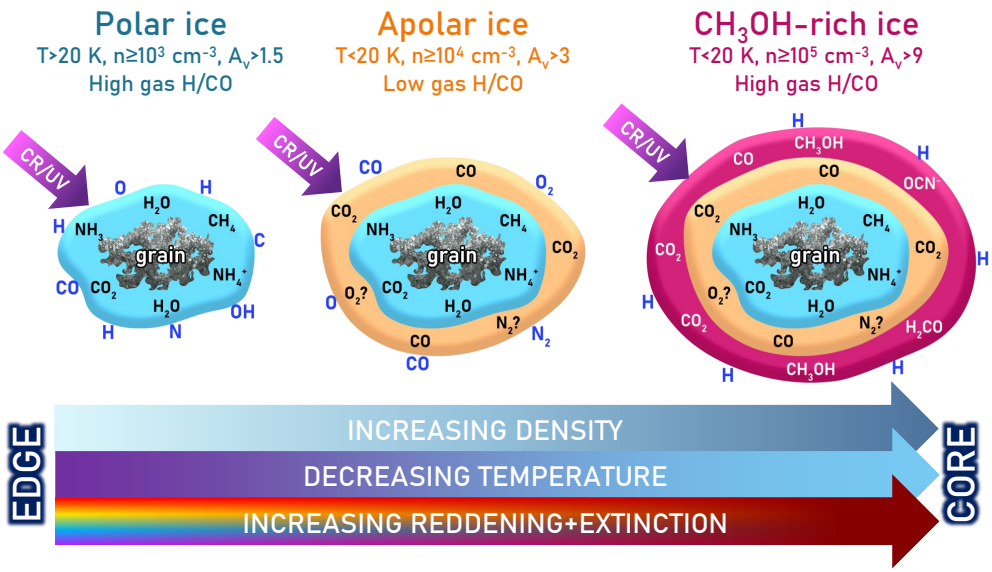

Figure 1.4: Different stages of ice growth in molecular clouds. In the first ice layers grown in the less dense translucent regions closer to the cloud edges, H_2O, CO_2, and hydrogenated species like NH_3 and CH_4 form. As densities increase, temperatures drop, enabling the growth of an apolar layer dominated by CO and CO_2. In the densest regions, CO is efficiently hydrogenated to form CH_3OH, resulting in a CH_3OH-rich layer that includes other species formed from CO like CO_2, OCS, and OCN^-.

layers. In this stage, CO also reacts with S- and N-species to respectively form OCS (Palumbo et al. 1997; Santos et al. 2024) and HNCO (Fedoseev et al. 2015), the latter of which is mostly consumed in acid-base reactions to form OCN^- (Novozamsky et al. 2001; van Broekhuizen et al. 2004). Laboratory experiments show that a myriad of other more complex and potentially prebiotically relevant organic molecules such as glycolaldehyde, methyl formate, glycerol, and propanol can form via CO hydrogenation as well (Chuang et al. 2016; Fedoseev et al. 2017; Qasim et al. 2019), although expected relative abundances of these species in the ices are low and, even when present, their weak IR signatures can be challenging to disentangle (*e.g.*, Chen et al. 2024).

This model of multiple chemically distinct ice growth stages shown in Fig. 1.4 is observationally supported in multiple ways. First, in clouds where multiple lines of sight with different densities can be probed, the lines of sight in denser regions show larger fractions of apolar species like CO and CO_2 in the total ice column density (Fig. 1.5). Furthermore, differences in x-intercepts when plotting various ice column densities in molecular clouds versus A_v (where the x-intercept of a given species indicates the minimum cloud density required for growth of that species in ices to begin) support a formation sequence where species like H_2O and CO_2 form first, followed by CO freeze-out and then CH_3OH formation at the highest A_v (see Fig. 7 in Boogert et al. 2008). Additionally, ice band profiles are sensitive to chemical environments (see Section 1.3.1), and the ice bands observed toward molecular clouds are consistent with multiple chemically distinct ice phases. However, the triphasic model described here is still only a simplified approximation of the complex chemical stratification expected

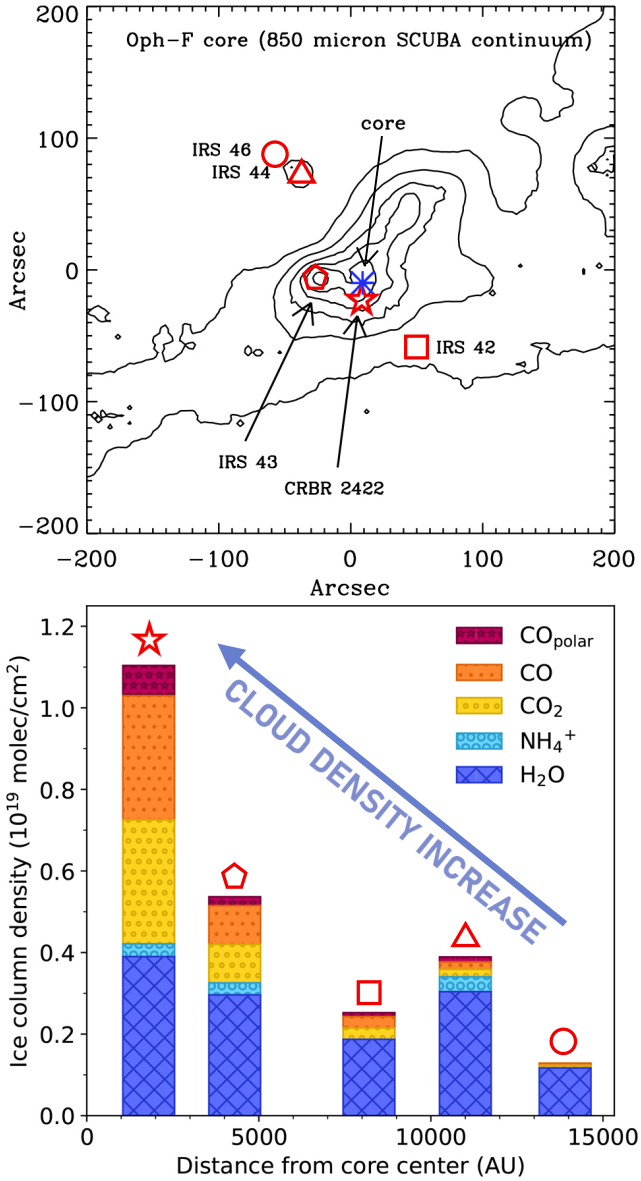

Figure 1.5: Spatial changes in ice column densities observed around the Oph-F cloud core. Top: 850 μm dust emission map of the Oph-F core. Blue star: core center; red shapes: 5 surrounding IR sources. Bottom: ice column densities observed toward the 5 IR sources in the Oph-F core. Lines of sight toward the outer, less dense core regions are dominated by water ice. Closer to the core center, the relative and absolute contributions of apolar species CO and CO_2 to the total ice column density increase. A significant column density of CO in a polar matrix (likely dominated by CH_3OH) is observed toward the source closest to the dense core.

within interstellar ices, and the transitions between the different ice phases are expected to be gradual rather than discrete as shown in Fig. 1.4.

Finally, it is important to note that the ice chemistry discussed thus far – the chemistry thought to be responsible for the formation of the cloud ice species presented in Fig. 1.3 – is primarily thought to be *non-energetic*, consisting of atom addition or acid-base reactions that do not require external energy input to proceed under interstellar conditions (Cuppen et al. 2024). However, it has long been proposed that *energetic processes* contribute to molecular cloud ice chemistry as well (Arumainayagam et al. 2019). Although dense molecular clouds are shielded from the external interstellar UV radiation field as discussed above, cosmic rays (high-energy ions and nuclei) are still able to penetrate the clouds and interact with the ice and gas within them. These cosmic rays can also generate a *secondary UV field* within the cloud by exciting local gas-phase H_2, which emit Lyman and Werner photons in the VUV range (6.9-13.6 eV) upon relaxation to ground state (Prasad & Tarafdar 1983). The UV flux expected from this process ($\sim 10^4$ photons cm^{-2} s^{-1}, Shen et al. 2004) is much lower than that of the interstellar UV field ($\sim 10^8$ photons cm^{-2} s^{-1}, Draine 1978), but it is nonetheless expected to trigger some photochemistry in the cloud ices.

Over the past few decades, plenty of laboratory experiments have shown that the sky is the limit when it comes to the molecules that can form via such energetic ice chemistry. Simulated cosmic ray or UV irradiation of interstellar ice analogs composed of the simple molecules in Fig. 1.3 can produce a myriad of more chemically complex and prebiotically relevant molecules, including heavy hitters like formamide, amino acids, and nucleobases (Munoz Caro et al. 2002; Bernstein et al. 2002; Kaňuchová et al. 2016; Öberg 2016; Oba et al. 2019; Chuang et al. 2022). However, no species of an indisputable energetic origin (*i.e.*, species that cannot form via non-energetic chemistry) have been detected in molecular cloud ices thus far (Boogert et al. 2015).

1.2.2 Protostars and protoplanetary disks

If a molecular cloud is sufficiently massive and dense, gravitational instabilities and turbulence can trigger the cloud's gravitational collapse, initiating the formation of a protostellar core. The nascent protostar then follows an evolutionary sequence that ultimately ends in the formation of a fully-fledged, hydrogen-fusing star in hydrostatic equilibrium.

In the case of low-mass stars (<8 M$_\odot$), the most common stars in our galaxy and the hosts of most known planetary systems, this evolutionary sequence lasts $\sim 10^6$-10^7 yr and can be roughly divided into four stages that are often conflated with spectroscopically defined *Classes* (Robitaille et al. 2006; Dunham et al. 2014). During the earliest stages following cloud collapse, an envelope of molecular cloud material as well as streamers from nearby clouds (Pineda et al. 2020; Valdivia-Mena et al. 2024) feed the core source. Gravitational potential energy is converted into thermal energy as the material collapses, heating the surrounding envelope in a thermal gradient that extends radially from the source. As temperatures rise, the dust within the heated parts of the envelope begins to thermally emit radiation that peaks in the far-IR and submillimeter ranges. Blackbody radiation from the central source itself is absorbed, re-radiated, scattered, and reddened by the surrounding envelope dust, extending the source spectral energy distribution (SED) into the IR range (Class 0). At this stage, the source is considered *deeply embedded* because most of its mass resides in its surrounding envelope rather than in the protostellar core source.

As the protostar continues to accrete surrounding envelope material, conservation of angular momentum results in outflows of accreted material from the source poles as well as the flattening of the inner portion of the envelope into a *protoplanetary disk*. Matter within the disk starts to coagulate into larger bodies, forming disk rings, gaps, and cavities, marking the beginnings of planetary formation (Segura-Cox et al. 2020). The envelope and disk continue to warm through source blackbody emission, and the SED profile of the source shifts to shorter wavelengths as envelope matter thins and the source grows hotter and more massive (Class I). Eventually the envelope material is completely depleted via outflows and accretion, leaving only the disk and a central pre-main sequence star that is hot and massive enough to be observable in the near-IR and visible ranges (Class II). Finally, the disk material is also depleted via disk winds and accretion by the source or disk planetesimals (Class III).

In the case of massive stars (>8 $M_\odot$), evolutionary stages during their formation are more difficult to define because they are more rare than low-mass stars in our galaxy, and their formation timescales are shorter ($\sim 10^5$ yr). Furthermore, massive protostars typically form in clusters where individual sources can be difficult to resolve. Nevertheless, their formation sequence also involves the gravitational collapse of a cloud, heating of the surrounding envelope material within which they are embedded, and formation of a disk (Beuther et al. 2007, 2025).

During the protostellar and protoplanetary disk stages, ices formed during the molecular cloud stage are inherited by the protostellar envelope and disk, where they can transform through various physical processes (Fig. 1.6). One of the processes most central to this transformation is the desorption of ice species into the gas phase, which is governed by molecular *snowlines*: the thermal boundaries that define the regions where envelope or disk temperatures become warm enough to sublimate specific ice species. Snowlines are not only important to accurately model the solid-state and gas-phase chemistry that occurs in envelopes and disks – they also govern the chemical composition of the planetesimals that form in the disk (see Section 1.2.3).

In younger and colder protostellar envelopes as well as the coldest, outermost regions of more evolved protostellar envelopes and the cold midplanes of protoplanetary disks, the molecular cloud ices can remain largely intact. As the ices move into warmer regions, they cross molecular snowlines in order of decreasing volatility, effectively *distilling* the ice layers as various ice species sublimate. Hypervolatile species like CO have snowlines around T$\sim$20 K and are the first to sublimate from the ices, water ice has a snowline around $T \sim 100$ K, and the snowlines of most of the other species shown in Fig. 1.3 are somewhere in-between. However, some species may still remain in ices past their snowlines if they are sufficiently *entrapped* within a matrix of ices with higher desorption temperatures. For example, some protostars with warmed envelopes and protoplanetary disks show CO profiles that are characteristic of CO trapped in ice matrices of less volatile species (like CO_2, CH_3OH, and H_2O, Pontoppidan et al. 2008; Cuppen et al. 2011; Bergner et al. 2024). For this reason, the water snowline is often considered the most important when modeling or analyzing gas-grain chemistry in protostellar envelopes and protoplanetary disks – given water's high abundance in ices, many ice species (especially less abundant ones like complex organics) are expected to be entrapped within a water-dominated matrix and thus co-desorb with water ice (Collings et al. 2004; Busch et al. 2022).

Before inducing desorption, warmer temperatures also increase the mobility of species within the ices, leading to ice restructuring. This restructuring explains the presence of pure CO_2 and CH_3OH ice features toward warmer sources: these species gradually *segregate* from

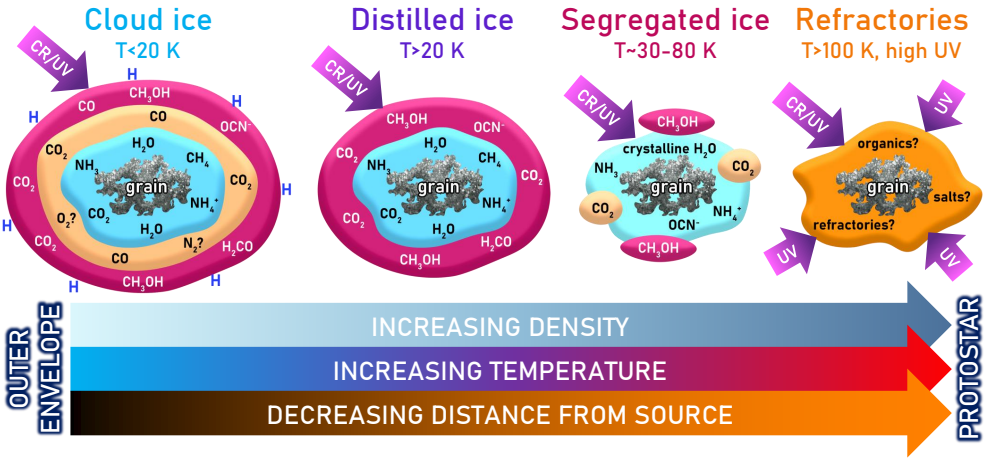

Figure 1.6: Changes in ice chemistry during thermal (and possibly energetic) processing in protostellar envelopes and protoplanetary disks. In the coldest envelope and disk regions, ice structures mimic those seen toward molecular clouds (see Fig. 1.4). As the ices move into warmer regions, hypervolatile species like CO desorb into the gas phase, distilling the ice. Even warmer temperatures drive the segregation of certain species (most notably CO_2) within the ice matrix and crystallization of the amorphous ices. Past 100 K, most of the volatile ices are expected to have desorbed into the gas, leaving behind on the grain more refractory species like salts and larger complex organics that may form via energetic processing.

other matrix constituents upon heating (*e.g.*, Ehrenfreund et al. 1998; Brunken et al. 2024b). Crystallization of amorphous ices is another form of ice restructuring that is observed toward warm sources, particularly in the case of water (*e.g.*, Dartois & d'Hendecourt 2001). Additionally, increased mobility can allow more species to overcome diffusion barriers and in turn increase rates of reactions that involve heavier species, such as recombination of radicals formed during ice energetic processing (Garrod & Herbst 2006) or acid-base reactions (van Broekhuizen et al. 2004). Although directly distinguishing ice species formed via thermally-driven diffusion is observationally challenging, chemical models often require diffusion to reproduce gas-phase abundances measured in the hot inner regions of protostellar envelopes, indirectly supporting their importance (*e.g.*, Garrod et al. 2008).

As is the case for molecular clouds, it is suspected energetic processing plays a role in the ice chemistry in protostellar envelopes and protoplanetary disks, both via the cosmic ray-induced secondary UV field and potentially the protostellar radiation field within certain envelope or disk regions. Although the latter internal UV field is expected to be very weak in the high-density envelope and disk midplane where most ices reside, ices that end up in less dense envelope regions close to the source or outflow cavity walls may experience UV fields with fluxes up to several orders of magnitude greater than the cosmic-ray generated field (Drozdovskaya et al. 2014). It has been suggested that a broad absorption feature in the 6-8 μm region isolated via empirical decompositions of protostellar spectra could be due to refractory organics produced by such UV irradiation of simpler ices, although purely thermal chemistry cannot be ruled out (Boogert et al. 2008). Such organics could potentially be refractory enough to survive past the water snowline and eventually serve to deliver volatile

elements into the inner solar system (see Section 1.2.3).

Finally, the journey of ice species within protostellar envelopes and protoplanetary disks is not expected to be linear in the sense of moving only in the direction of colder to warmer, ice phase to gas phase. Some degree of thermal cycling within the envelope is expected due to events like accretion bursts (see Chapter 2). Furthermore, accreted disk material can be transported from hotter to colder disk regions via outward radial or inward vertical diffusion and viscous spreading, especially in early stages when disk pressures are high and grain sizes are small (*e.g.*, Stevenson & Lunine 1988; Yang et al. 2013; Williams et al. 2025). Thus, interstellar volatiles can cycle multiple times between the ice and gas phase throughout the evolution of a protostellar system.

1.2.3 Planetary bodies

The disk snowlines discussed in Section 1.2.2 are a key factor that partially dictates the compositions of planetary objects based on their formation locations within the disk. Namely, a given species can be accreted by planetesimals that form outside of the snowline of that species, so the starting material that forms a planetary body will depend on where that body lies in the protoplanetary disk in relation to molecular snowlines. This initial chemical record is subsequently altered as snowlines change due to gradual dissipation of the protoplanetary disk and as planetary bodies undergo scattering and collision events due to dynamic interactions with other bodies. Geologic, atmospheric, or space-weathering processes on the planetary bodies further alter the chemical record once the protoplanetary disk has fully dissipated.

In our solar system, small airless bodies that formed in the outermost reaches of the solar system are thought to contain some of the most pristine records of inherited volatiles from interstellar ices because their small sizes preclude significant geologic or atmospheric processing, and their formation locations in the outer solar system allowed them to retain considerable amounts of volatiles after their formation. Comets are a prime example, and the outgassing of volatiles in their comae allow for direct comparisons between their volatile inventories and those of interstellar ices and protostellar gases, which have revealed some striking similarities (Öberg et al. 2011; Drozdovskaya et al. 2019, see also Chapter 4). However, systematic differences between cometary and interstellar volatile abundances as well as the presence of crystalline silicates in cometary dust (Zolensky et al. 2006) also point toward cometary material undergoing at least some degree of chemical processing within the protoplanetary disk.

The isotopic ratio of deuterium to hydrogen (D/H) in water is particularly sensitive to physicochemical conditions. Thus, this ratio has been used to evaluate the extent to which protostellar water is processed in the disk before it is accreted by comets (Persson et al. 2014; Cleeves et al. 2014). Interpretations of these comparisons are complicated by the large scatter in water D/H observed in both cometary and protostellar values (*e.g.*, Paganini et al. 2017; Jensen et al. 2019), as well as potential fractionation effects during cometary ice sublimation (Mandt et al. 2024). Furthermore, protostellar gas water D/H values have often been used as a proxy for ice D/H values because HDO ice could not be robustly detected toward protostars prior to JWST, but gas-phase reprocessing may cause differences in ice and gas D/H values. Chapters 2 & 3 of this thesis present the first reliable detections of protostellar HDO ice and calculations of protostellar water ice D/H values, marking an important advance in our ability to characterize how water chemically evolved during its journey from the interstellar medium to outer solar system bodies. The measured ice values in these chapters show agreement with

the highest protostellar envelope and protoplanetary disk water gas D/H values on the order of $\sim$ a couple 10^{-3}. These values are elevated by factors of $\sim$2-10 with respect to cometary water D/H values that are typically on the order of 10^{-4}, which could indicate either some level of chemical reprocessing of interstellar water ice within our past protoplanetary disk or a diversity in interstellar water ice D/H values that reflect differences in prestellar temperatures, densities, or timescales (see Chapters 2 & 3 for further discussion).

Isotopic ratios have also been used to argue an interstellar origin for some of the organic molecules found on carbonaceous chondrite meteorites, which originate from carbonaceous asteroids. Today these bodies are primarily found in the asteroid belt between Mars and Jupiter, but they may have been dynamically scattered there from a location further out (perhaps as far as where Saturn formed, Alexander 2017). Their high carbon abundances and signatures of past water presence indicate they inherited significant quantities of volatiles from the protoplanetary disk, although these volatiles were likely less chemically pristine than those inherited by comets given the more inward formation locations. Accretion of the radiogenic isotope ^{26}Al by these bodies also caused secondary parent body processes like aqueous alteration and thermal metamorphism that further changed their chemical inventories. Nevertheless, the high D/H ratios of organics present on carbonaceous chondrites point to possible origins within ices either in the interstellar medium or in the outermost regions of the protoplanetary disk. Specifically, energetic processing of simpler organic ices in these regions has been suggested as a possible pathway to produce the highly refractory and chemically complex insoluble organic matter found in carbonaceous chondrites (Alexander et al. 2007).

1.3 Infrared spectroscopy of ices

Molecular spectroscopy is the study of how molecules interact with light. These interactions are governed by the laws of quantum mechanics, whereby molecules can absorb or emit photons by transitioning between their quantized electronic, vibrational, or rotational energy states. Transitions from lower to higher energy states result in photon absorption, whereas transitions from higher to lower energy states result in photon emission. The energy difference between the molecular energy levels involved in a transition defines the energy (*i.e.*, wavelength) of the emitted or absorbed photon (Fig. 1.7). Electronic transitions typically correspond to the energy of UV to visible photons, vibrational transitions to infrared (IR) photons, and rotational transitions to microwave and radio photons.

Molecules in space can be identified and quantified by their unique emission or absorption features in telescopic spectra. The vast majority of interstellar molecules have been observed in the gas phase via emission lines at millimeter or centimeter wavelengths – *i.e.*, rotational spectroscopy (McGuire 2022). This spectral range is particularly useful for interstellar observations in part because little thermal energy is required to populate excited rotational levels due to their small energy gaps, so molecular emission lines can often be detected even in very cold environments (*e.g.*, Kaifu et al. 2004). However, in the case of ices, confinement within a solid matrix restricts their rotational motion, making them unobservable with rotational spectroscopy. Instead, the ice chemistry described in Section 1.2 has been uncovered entirely using IR wavelengths – *i.e.*, vibrational spectroscopy.

The vibrational transitions of a molecule are associated with *vibrational modes*, which

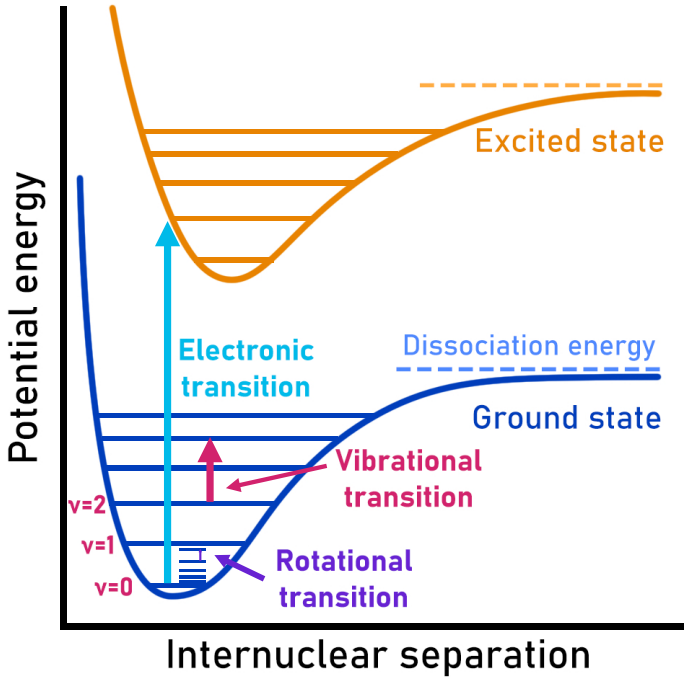

Figure 1.7: Electronic, vibrational, and rotational transitions shown in a molecular potential energy well diagram. The energy gap between the two levels involved dictate the wavelength of light that is emitted or absorbed during a transition.

correspond to specific motions of the molecule's atoms relative to each other. Every molecule has a certain number of *fundamental modes* that arise from transitions between a ground vibrational state v=0 and the first excited state v=1. Examples of fundamental modes include stretching, bending, or twisting motions as shown in Fig. 1.8. Transitions between ground states and excited states $v \geq 2$ are called *overtones*, and *combination modes* arise when a single photon induces two transitions simultaneously. Additionally, collective vibrations of molecules bound together in a solid or liquid result in *librations* and *lattice modes*. Fundamental modes typically produce the strongest observed features, whereas overtones, combination modes, and lattice modes are weaker and thus more difficult to observe unless the carrier molecule is very abundant.

Not all vibrational modes can be observed. As dictated by spectroscopic selection rules, only the vibrational modes in which the molecule's dipole moment changes as a result of the vibration will result in the absorption of an IR photon. These modes are referred to as *IR active*. Modes that result in no net dipole moment change, *IR inactive* modes, will therefore not appear in IR spectra. For some molecules, this means that only some of their vibrational modes can be observed; others, like homonuclear diatomics, have no IR active vibrational modes and thus cannot be observed in the IR (unless they are bound within a matrix that induces a weak dipole between the two atoms). As a result, the presence of molecules like N_2 and O_2 in interstellar ices cannot be spectroscopically confirmed nor well-constrained,

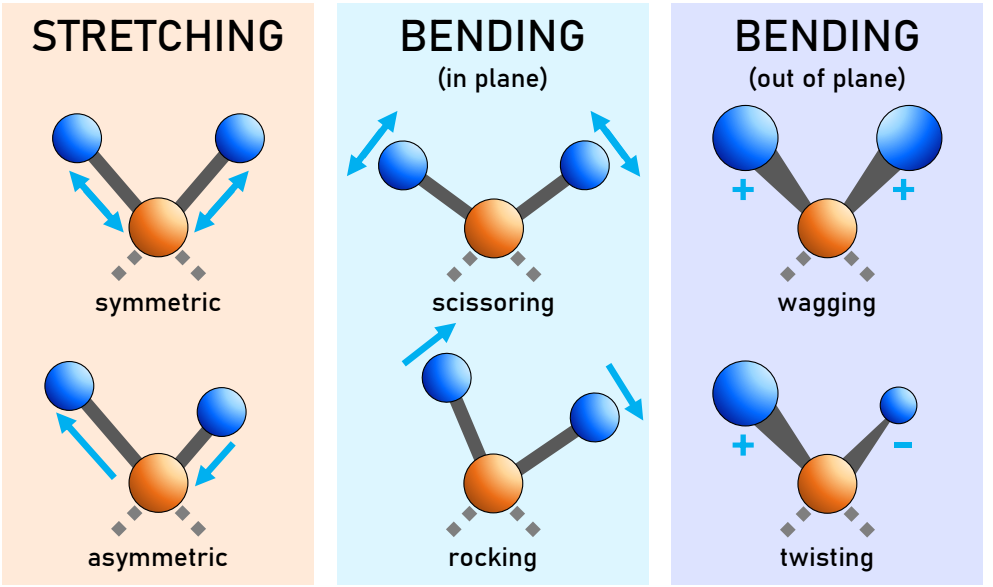

Figure 1.8: Six examples of fundamental molecular vibrational modes.

although it is strongly suspected (Ehrenfreund & van Dishoeck 1998; van Dishoeck et al. 2025).

The specific peak positions, profiles, and intensities of IR vibrational modes observed toward interstellar regions contain a wealth of information about the chemical identities, quantities, and even the physical and chemical environments of the molecules present in the ices. Extracting this information requires an integrated approach in which observations are compared to models that employ laboratory data. The following sections explain how both observational and laboratory data of such ices are acquired and analyzed.

1.3.1 Observational methods

Fig. 1.9 provides a schematic of the observing geometry used to acquire interstellar ice spectra. The telescope is aimed toward an IR light source, which can be either an extincted background star located behind the interstellar cloud of interest, or it can be a protostar that is embedded within the cloud. Molecular absorptions or emissions from species located along the line of sight from the light source to the telescope are then observed against the (proto)stellar continuum. In the case of background stars behind molecular clouds, cold ice bands are observed in addition to lines from gaseous species within the background star's photosphere (*e.g.*, McClure et al. 2023). In the case of protostars, the line of sight typically follows a thermal gradient where temperature decreases with distance from the protostar. Thus, species detected toward protostars can include pristine ices in the colder outer regions of the envelope, thermally-processed ices in the warmer inner regions of the envelope, and gas-phase molecules in the hot core region closest to the source (*e.g.*, van Dishoeck et al. 2025). Additionally, the line of sight in ground-based data includes absorptions from IR-active species

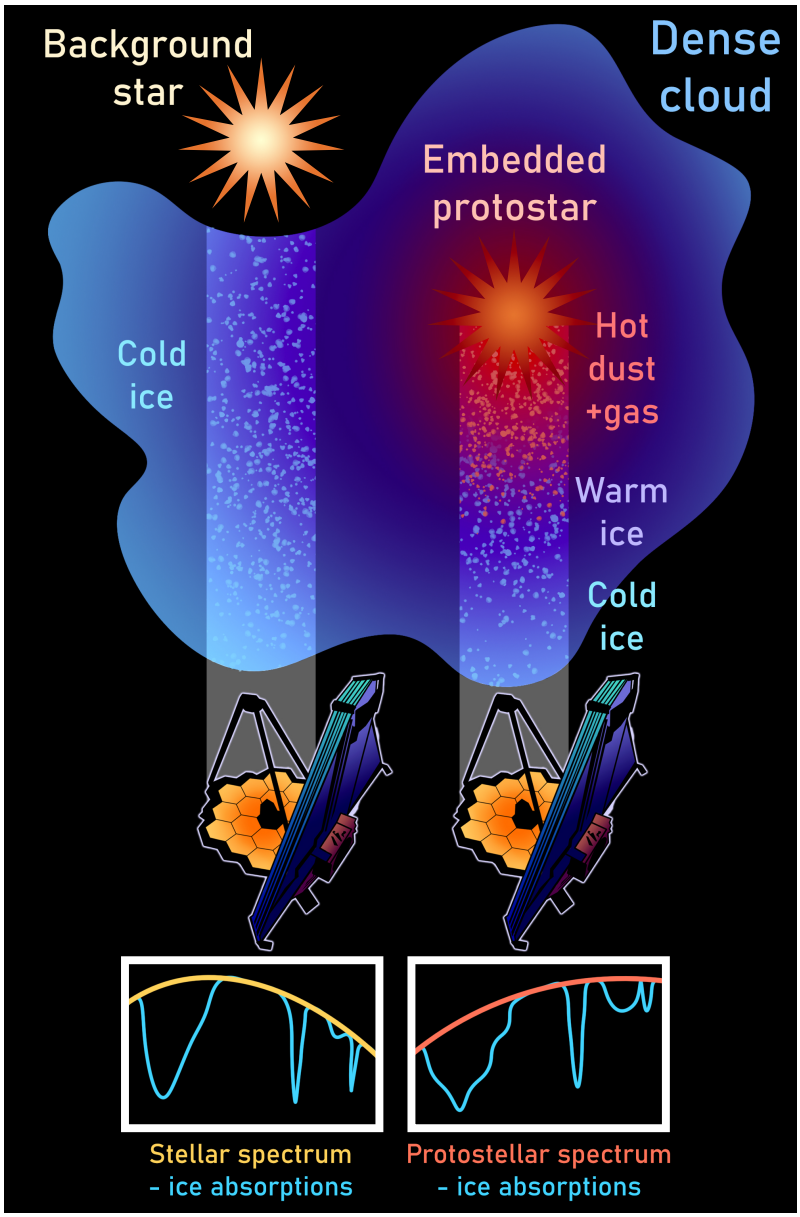

Figure 1.9: A schematic of how telescopes observe absorption features of interstellar ices in dense clouds and protostellar envelopes. The ices are observed along a pencil beam that traces the path from an IR light source (either an extincted background star or a protostar) to the telescope.

in Earth's atmosphere like CO_2 and H_2O; space-based telescopes eliminate this contaminant from the line of sight and are thus considered optimal for observing interstellar ices, although ground-based data remains valuable for analyzing interstellar ice features in spectral windows

free of atmospheric contaminants and can often offer higher spectral resolution than space-based telescopes in these windows (*e.g.*, Pontoppidan et al. 2003; Boogert et al. 2022).

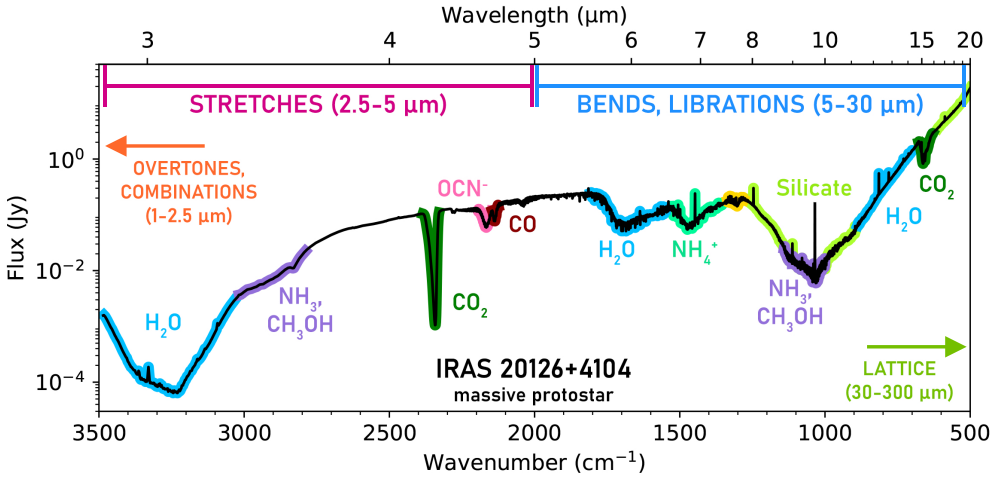

Figure 1.10: Example IR spectrum of a massive protostar (IRAS 20126+4104) showing interstellar ice and dust absorption features upon the protostellar continuum.

An example mid-IR (2.5-30 μm) spectrum of interstellar ices observed toward a protostar is presented in Fig. 5. This spectral window is dominated by fundamentals, specifically stretching modes from 3-6 μm and bending and libration modes from 6-30 μm. The near-IR region (1-2.5 μm) is dominated by weak combination and overtone features. The far-IR region (30-300 μm) is dominated by lattice modes. Almost all ice IR features are observed in absorption because the thermal energy required to significantly populate excited vibrational states of ices typically exceeds ice binding energies and would lead to ice desorption, with the exception of a few low-energy lattice modes in the far-IR that are occasionally observed in emission (*e.g.*, Omont et al. 1990).

A specific molecule can be identified or "assigned" in an interstellar IR spectrum if its characteristic IR features, defined via controlled laboratory experiments or theoretical quantum calculations, are observed. Sometimes, assignments to specific molecules are not trivial because molecules that share chemical functional groups (*i.e.*, bond structures) often have similar or overlapping IR signatures. In the case of such a degeneracy, the presence or absence of other characteristic features of the assigned molecule (or its isotopolog) can corroborate or refute the assignment. Assignments can also be ascertained by comparing how closely observed parameters like peak position and full width half maximum match those in laboratory data. Attempts have been made to establish a classification scheme that characterizes the reliability of ice feature assignments using terms like *secure*, *likely*, or *tentative* based on a set of criteria (Boogert et al. 2015), but use of these criteria is not standardized across the current literature (*e.g.*, Öberg et al. 2011; Rocha et al. 2024).

Once assigned, an IR peak can be used to quantify the *column density* of a molecule along the line of sight. Column density N is defined as the density of molecules n integrated along a given path ℓ, in this case the line of sight:

$$N = \int n \, d\ell \tag{1.1}$$

To obtain N of a given species from an observed IR feature, a portion of the observed spectrum that contains the feature must first be converted from the flux scale to the optical depth τ scale via the equation:

$$\tau = -ln(I/I_o) \tag{1.2}$$

where I is the observed flux, and I_o is the modeled (proto)stellar continuum flux without ice absorptions. I_o can be modeled using template stellar spectra, extincted blackbody curves, or polynomial fits to manually-defined continuum points. N can then be calculated via:

$$N = \frac{\int_{\nu_1}^{\nu_2} \tau_\nu \, d\nu}{A} \tag{1.3}$$

where the numerator of the fraction represents the integrated optical depth of the IR feature over a defined frequency range $\nu_1 - \nu_2$ expressed in wavenumbers (cm^{-1}) and A is the experimentally-determined *band strength* of the feature (discussed further in Section 1.3.2).

In addition, observed IR feature profiles can be used to infer the physical and chemical properties of their ice carriers. This is because intermolecular interactions (*e.g.*, hydrogen bonds, van der Waals forces) with surrounding matrix species can affect a molecule's electron density and geometry (*i.e.*, bond lengths and angles), altering its vibrational energy levels and, in turn, the peak properties of its IR features – most notably position and width. Fig. 1.11 presents two examples of how IR profiles of ices change with physical and chemical environments in the case of H_2O (left) and CO_2 (right) ices, respectively.

The top left panel presents the 3 μm O-H stretching mode in three pure H_2O laboratory ices with different morphologies: porous amorphous, compact amorphous, and crystalline. The feature appears significantly broader in the amorphous samples than in the crystalline sample. The narrowing of ice IR features upon transitions from amorphous to crystalline morphologies is observed in many species because crystalline structures have less disorder and thus less possible configurations of molecules within the matrix – more possible configurations result in a larger distribution of possible electron densities, bond distances, and angles, leading to peak broadening in amorphous ices (Mastrapa et al. 2009). In the case of the 3 μm H_2O band, the crystalline peak position is also significantly redshifted from the amorphous peak positions. Such band profile differences can be exploited when analyzing observations to determine whether the ice along the line of sight is amorphous or crystalline (*e.g.*, Smith et al. 1989). For example, the bottom left panel shows the 5 μm continuum flux map of an intermediate-mass protostar, HOPS 370, from the NIRSpec instrument aboard JWST (see Section 1.3.1). Two spectra (middle left panel) are extracted from the datacube: one using an aperture centered on a shocked knot (Tyagi et al. 2025) in the inner regions of the envelope close to the protostar, and one using an aperture centered on an outer part of the envelope illuminated by scattered light in the outflow cavity. The 3 μm water feature in the spectrum extracted closer to the protostar shows a greater relative contribution of crystalline water ice and a lesser relative contribution of amorphous water ice, demonstrating how thermal processing in the warmer, inner regions of the protostellar envelope crystallizes water ice.

The top right panel of Fig. 1.11 presents the 4.4 μm asymmetric stretching mode of the

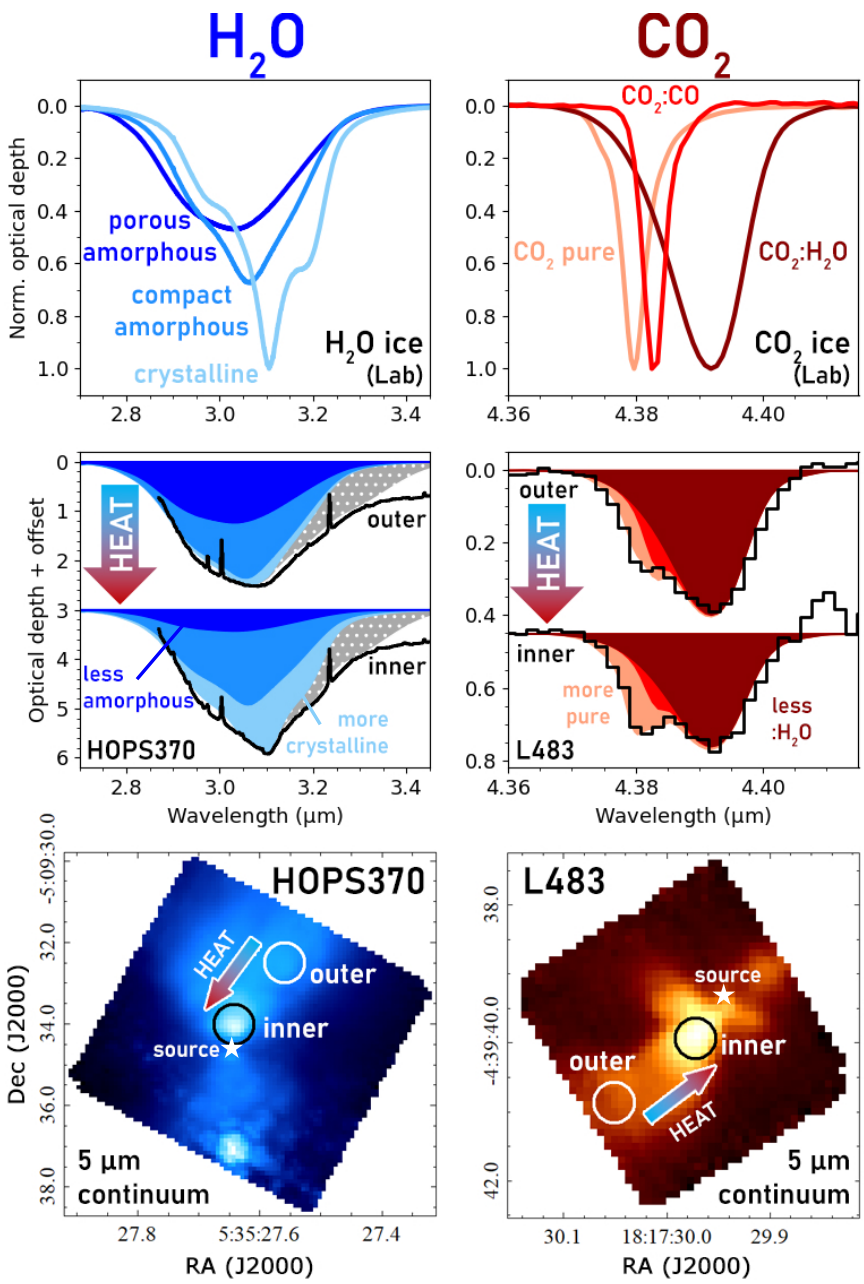

Figure 1.11: Differences in band profiles of H_2O (left) and CO_2 (right) ices caused by changes in ice morphology (left) and chemical environment (right). Top: laboratory spectra. Middle: observed protostellar spectra. Bottom: continuum maps showing the protostellar regions from which the spectra in the middle panels were extracted.

$^{13}CO_2$ isotopolog in three laboratory ices containing CO_2: a pure CO_2 ice, a mixed CO_2:CO ice, and a mixed CO_2:H_2O ice. The peak position and profile of the band differ significantly between the three chemical environments. Such profile changes are often most drastic between polar and apolar matrices (*i.e.*, matrices with and without hydrogen bonds), where polar matrices often result in broader IR features due to greater intermolecular forces that affect the dipole moments of the embedded molecules of interest (Ehrenfreund et al. 1997). Such differences can again be exploited to determine the chemical environments of various interstellar ice species (*e.g.*, Boogert et al. 2000). For example, the bottom right panel shows the 5 μm continuum flux map of a low-mass protostar, L483, from the NIRSpec instrument aboard JWST (see Section 1.3.1). Two spectra (middle right panel) are extracted from the datacube: one using an aperture centered on a bright spot in the outflow in the inner regions of the envelope close to the protostar, and one using an aperture again centered on an outer part of the envelope illuminated by scattered light in the outflow cavity. The 4.4 μm $^{13}CO_2$ feature in the spectrum extracted closer to the protostar shows a greater relative contribution of pure CO_2 ice and a lesser relative contribution of CO_2 ice mixed with water, demonstrating how thermal processing in the warmer, inner regions of the protostellar envelope promotes segregation of CO_2 from the previously mixed ice matrix.

The size, shape, and mineralogy of an icy dust grain can also influence the profiles of its ice features. Grain shape and size effects are most pronounced in strong and sharp features of the most abundant ices (Dartois & d'Hendecourt 2001; Dartois et al. 2022). These effects can be modeled using ice opacities generated from optical constants of laboratory ices, rather than the laboratory ice absorbance spectra often used to empirically fit weaker ice features. Such effects become increasingly important to account for as grain sizes grow (Dartois et al. 2024).

JWST

A large portion of the observational work utilized in this thesis was collected with the *James Webb* Space Telescope (JWST), which launched on December 25, 2021, approximately a month before this thesis work began.[1]

Prior to JWST, most of the IR spectra that informed the ice chemistry models laid out in Section 1.2 were collected either using the Infrared Space Observatory (ISO, 1995-1998) or the *Spitzer* Space Telescope (2003-2020). The short- and long-wavelength spectrometers on board ISO covered a broad spectroscopic range (2.5-200 μm) and provided moderate spectral resolving power in the mid-IR (R∼800-3000), but its low sensitivity (a few Jy) limited the sources that could be observed to the brightest massive objects (Gibb et al. 2004). *Spitzer* offered a sensitivity improvement of several orders of magnitude, creating a new opportunity to observe fainter low-mass protostars as well as more extincted background stars (Öberg et al. 2011). Nevertheless, the spectral range of its IR spectrograph (5-37 μm) neglected to cover the essential 2-5 μm spectral region where several major ice features lie, and its low spectral resolving power below 10 μm (R∼100) made it impossible to fully resolve narrow ice features or disentangle ice absorptions from gas phase emissions.

The combination of the Near-Infrared Spectrograph (NIRSpec) and the Mid-Infrared Instrument (MIRI) aboard JWST offers spectral coverage from 0.6-28 μm with comparable resolving power to ISO (R up to 2700 in the near-IR and up to 3500 in the mid-IR) and sensitivity orders of magnitude better than *Spitzer* (10^{-3}-10^{-2} mJy in the near-IR, 10^{-2}-10^{-1}

[1] Christmas day was a fitting launch date, as the results from this telescope have been an immense gift to the field.

mJy in the mid-IR). Furthermore, integral field units (IFUs) can be used to collect spatially resolved spectral datacubes with angular resolution on the order of up to ∼0.1", enabling the mapping of ice absorptions in the case of sources with extended emission.

In addition to the work discussed in this thesis, the improved capabilities of JWST have over the past few years led to observations of various weak features attributed to complex organic molecules (*e.g.*, Rocha et al. 2024; Chen et al. 2024; Nazari et al. 2024) as well as previously unobservable overtones and dangling modes of major ice species (*e.g.*, Brunken et al. 2024a; Noble et al. 2024) in protostellar envelopes. They have also enabled more comprehensive characterizations of the chemical environments of ices and the detection of trace ice species like NH_3, OCN^-, OCS, and $^{13}CO_2$ in dense clouds with record-high extinctions (*e.g.*, McClure et al. 2023) and Class II protoplanetary disks (*e.g.*, Sturm et al. 2023; Bergner et al. 2024). And finally, data from the IFUs have revealed changes in ice morphology throughout protostellar envelopes on spatial scales that were previously unresolvable in the IR (*e.g.*, Tyagi et al. 2025).

1.3.2 Laboratory methods

Laboratory measurements provide experimental data that is essential to interpreting the observations of ices described in Section 1.3.1. In such experiments, interstellar ice analogs with precisely controlled compositions are deposited upon a cryo-cooled flat substrate within an ultrahigh vacuum chamber with typical pressures on the order of $\leq 10^{-8}$-10^{-10} mbar. The resulting thin ice slab grown on the substrate is a physical approximation of the thin ice layers on top of interstellar dust grains observed toward background stars and protostars. When an IR-transmissive material (*e.g.*, KBr, CsI, Ge) is used as the substrate, an IR spectrum of the deposited ice can be collected in transmission using a Fourier-transform IR spectrometer (FTIR) whose beam path travels through the substrate and the ice layers deposited on top of it. This geometry is in some ways comparable to the transmissive observing geometry displayed in Fig. 1.9. Some UHV setups optimized for investigating interstellar ice chemistry utilize metal reflective substrates instead (*e.g.*, gold) to collect spectra in reflection-absorption mode at grazing incidence angles. This geometry yields greater sensitivity for the purpose of detecting extremely weak features or trace reaction products, but the resulting spectra are not directly comparable to observations.

The thickness of the deposited ice can be measured using the principles of thin film interference. A laser beam is aimed at the ice, and the intensity of the reflected beam is measured. During the deposition of the ice, the intensity of this reflected beam oscillates depending on the ice thickness due to the portion of laser light that is immediately reflected at the vacuum-ice interface interfering with the portion of laser light that is refracted at the vacuum-ice interface and reflected at the ice-substrate interface (see Fig. 1.12). Intensity maxima, resulting from constructive interference of the two interacting beams, are achieved at ice thicknesses d dictated by the following equation:

$$d = \frac{m\,\lambda}{2\sqrt{n^2 - sin^2\theta}} \tag{1.4}$$

where m is the integer number of constructive interference fringes, λ is the wavelength of the laser beam, n is the ice refractive index at wavelength λ, and θ is the angle of incidence

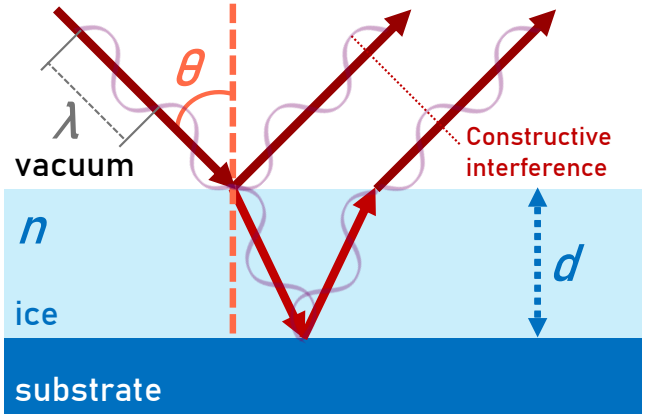

Figure 1.12: Schematic demonstrating the principle that results in an interference pattern when light is reflected off a growing thin film. The case of constructive interference is shown; changing the thickness of the ice d will result in changes in the observed interference.

of the laser beam. The refractive index n of the ice can be obtained by measuring the interference pattern of two laser beams positioned at two different incidence angles during an ice deposition using the following equation:

$$n = \sqrt{\frac{sin^2\theta_1 - \gamma^2 sin^2\theta_2}{1-\gamma^2}} \tag{1.5}$$

where θ_1 and θ_2 are the respective angles of incidence of the two laser beams and γ is equal to the ratio of the respective periods T_2/T_1 of the two resulting interference patterns.

The thickness of an ice can then be used to calculate the apparent band strength A' of various IR absorption features of a given ice species:

$$A' = \frac{M\,\ell n 10}{\rho\, d\, N_A} \int_{\nu_1}^{\nu_2} abs_\nu \, d\nu \tag{1.6}$$

where M is the molar mass of the ice species, ρ is the ice density, d is the thickness calculated from Eq. 1.3.2, N_A is Avogadro's number, and the integral is the absorbance of the ice feature of interest integrated over frequencies ν_1-ν_2 expressed in wavenumbers. The ice density ρ can be obtained from measurements using a *quartz crystal microbalance*, which detects extremely small changes in mass during ice deposition upon a quartz crystal substrate via changes in the crystal's resonance frequency (Allodi et al. 2013).

The laboratory IR spectra collected in such experiments can be directly compared to ice observations to identify the chemical species present in ices, and their column densities can be quantified using A' values. This empirical treatment is usually sufficient for analyzing ices observed toward dense clouds and Class 0 and I protostars, *i.e.*, the pencil-beam scenario. In the case of more evolved Class I or II protostars with hefty, optically thick disks, the photon paths toward the observer are less straightforward and thus require radiative transfer models that use ice optical constants as input rather than ice absorbance spectra (*e.g.*, Sturm et al.

2023; Bergner et al. 2024). Additionally, the profiles of strong and sharp ice features of the most abundant ice species (*i.e.*, H_2O, CO_2, CO) can differ significantly between the laboratory thin ice slab scenario and the interstellar ice layer on a μm-sized dust grain scenario due to spectral contributions from scattering, especially when grain sizes grow large. In such cases, the observed ice absorptions require modeling via their optical constants, which can be calculated from laboratory ice slab absorbance spectra (*e.g.*, Baratta & Palumbo 1998; Gerakines & Hudson 2020). The work in this thesis primarily focuses on less abundant ice species and younger, less geometrically complex observational targets. Therefore, ice optical constants are not measured nor extensively utilized – with the exception of Chapter 3, in which H_2O ice optical constants were used to account for scattering effects in the H_2O ice bands when calculating HDO/H_2O ice ratios toward a Class 0/I source with a disk.

IRASIS

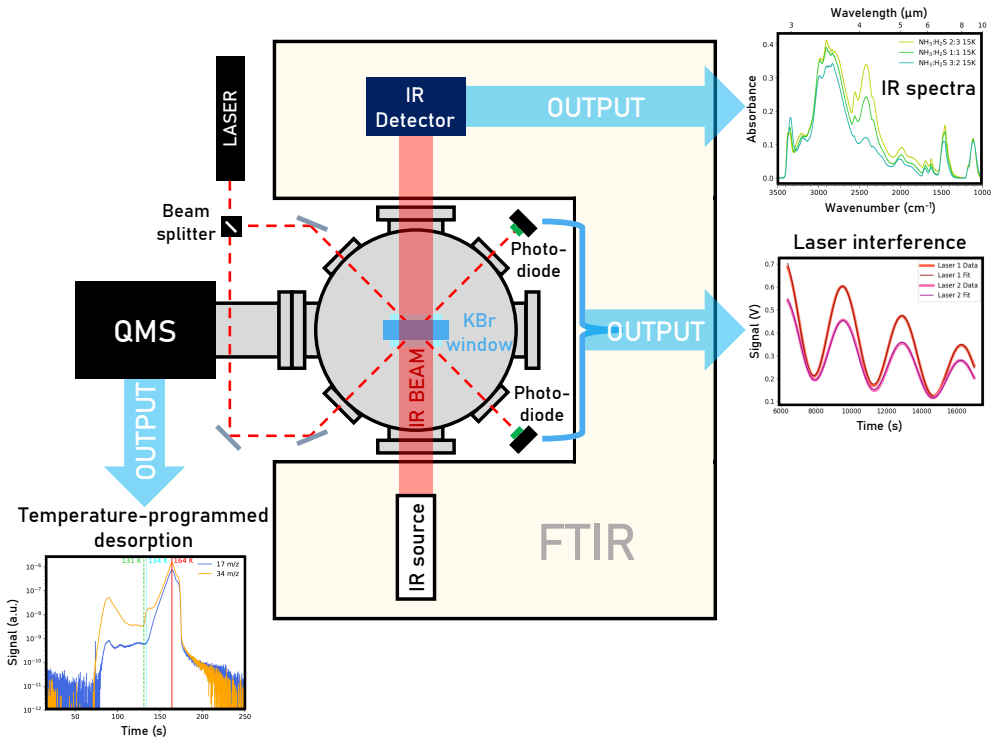

Figure 1.13: Top-view schematic of IRASIS in the configuration used during the work in this thesis.

The Infrared Absorption Set-up for Ice Spectroscopy (IRASIS) is an ultrahigh vacuum (UHV) setup in the Leiden Laboratory for Astrophysics (Rachid et al. 2021) that was used in this thesis to obtain experimental transmission spectra and band strengths of interstellar ice analogs. Its central chamber has a base pressure of $<1\times10^{-9}$ mbar, corresponding to a density on the order of $\sim10^{7}$ molecules cm^{-3}. Fig. 1.13 presents a schematic of the setup.

At the center of the UHV chamber, an IR-transmissive window substrate is attached to the arm of a cryostat that is capable of cooling the window down to ∼12 K. Both KBr and Ge substrates were used in the setup during the work presented in this thesis. The temperature of the substrate can be controlled from 15 K to room temperature via a resistive heater attached close to the substrate on the cryostat arm. The heater output is managed via proportional-integral-derivative control with a LakeShore controller to achieve a desired temperature or ramp rate (usually ∼0.4-1 K min^{-1}) in the case of warm-up experiments.

Ice samples are grown on both sides of the cryo-cooled substrate simultaneously by dosing gases and vapors of species of interest into the chamber via three leak valves, each attached to three independent gas manifold lines. This system enables controlled background deposition of ice mixtures containing up to three different chemical species. Using separate dosing lines for each species significantly improves accuracy in the reported mixing ratios compared to previous versions of the system, in which species were pre-mixed in the gas manifold and entered the chamber together through a single leak valve (*e.g.*, Terwisscha van Scheltinga et al. 2018). More detailed discussions of the benefits of using independent dosing lines to deposit ice mixtures can be found in the appendix of Chapter 6 as well as Yarnall & Hudson (2022).

This substrate lies normal to the path of a collimated infrared beam generated by an FTIR, which passes into and out of the chamber through two ZnSe windows parallel to the substrate. With this geometry, IR spectra are collected in transmission mode, directly comparable to the ice transmission spectra collected in astronomical observations. The chamber also includes four smaller ZnSe windows that enable laser interference measurements of ice sample growth and thickness. Two visible laser beams enter the chamber, one on each side of the substrate, and reflect off the substrate at 45° incidence into two photodiode detectors outside the chamber. The experiments presented in this thesis employed either a 633 or 543 nm HeNe laser, depending on the wavelength at which visible refractive index values were available for a given ice of interest.

Additionally, a quadrupole mass spectrometer (QMS), which can monitor the gas-phase species in the chamber during experiments, is positioned at 90° with respect to the IR beam path. The two primary purposes of the QMS on IRASIS are 1) leak valve calibration to yield ices with specific column densities and mixing ratios, and 2) temperature-programmed desorption (TPD) experiments. The QMS can also be used to detect IR-inactive contaminants during deposition, evaluate the cleanliness of the chamber prior to an experiment, and identify any possible solid-state reaction products during desorption.

Multiple procedures exist for leak valve calibration via the QMS. A procedure for depositing ice mixtures including only species that are either gaseous or have high vapor pressures at room temperature is described in Chapter 5; a procedure for depositing ice mixtures including species with extremely low vapor pressures at room temperature (*e.g.*, formamide) is described in Chapter 6.

During experiments that include TPD, the QMS monitors gas-phase species in the chamber as the ice sample is warmed at a constant rate. Once ices in the sample reach their desorption temperatures and sublimate, they are detected by the QMS. Thus, TPD experiments can yield the desorption temperatures or trapping efficiencies of ice species in various chemical environments. Because heating timescales in these experiments are orders of magnitude slower than the heating timescales (10^4-10^6 years) experienced by ices in environments like protostellar envelopes (Viti & Williams 1999), the laboratory desorption temperature of a given

species will be higher than its interstellar desorption temperature (Brown & Bolina 2007).

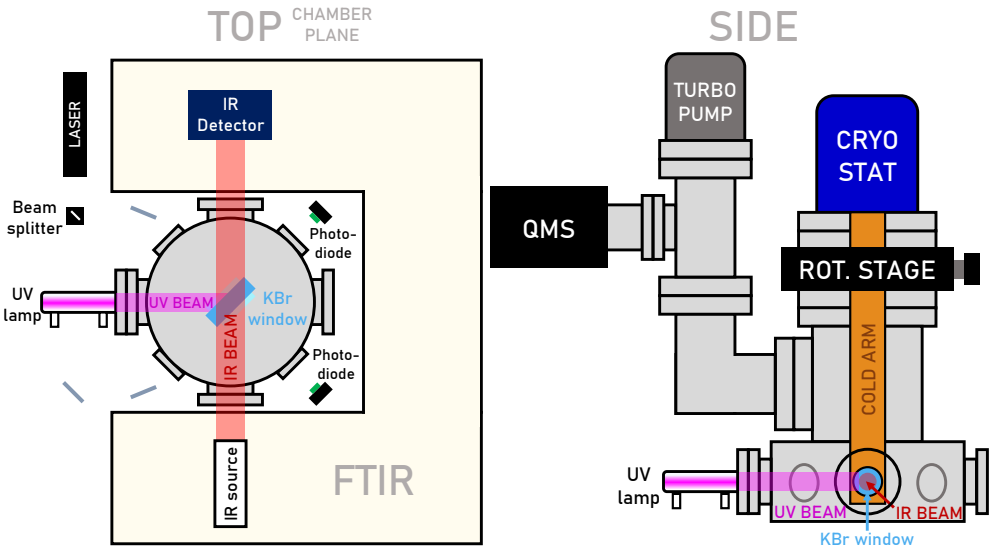

Figure 1.14: Top- and side-view schematics of IRASIS in the updated configuration that enables ice sample UV irradiation.

Following the work done in Chapters 2-6, IRASIS was upgraded to enable the IR characterization of species formed via UV irradiation of interstellar ice analogs. A schematic view of the chamber after this upgrade is presented in Fig. 1.14. Am F-type microwave discharge hydrogen-flow lamp (MDHL) replaced the QMS on the port perpendicular to the IR beam windows, and the QMS was moved to a port further from the sample and closer to the system turbomolecular pump. The MDHL generates Lyman-α photons at 121.6 nm as well as a broader molecular hydrogen emission profile centered around 160 nm (Ligterink et al. 2015).

To irradiate the ice sample, the substrate can be rotated via the chamber rotational stage to be either oblique (usually 45°) or perpendicular to the impinging UV beam. In the former case, collection of IR spectra can proceed simultaneously with UV irradiation, but longitudinal optical (LO) modes will be present in the spectra (Palumbo et al. 2006). The ice thickness cannot be monitored with laser interference in either of these geometries, so the ice sample is typically deposited with the substrate positioned perpendicular to the path of the IR beam (as shown in Fig. 1.13) before the sample is rotated for UV irradiation. It is important to note that with this geometry, only one side of the substrate is irradiated because KBr is opaque at the UV wavelengths generated by the lamp, which must be taken into account when yields are calculated.

1.4 Thesis overview

1.4.1 Aims

Since the first successful observation of interstellar ices in the Orion Nebula half a century ago (Gillett & Forrest 1973), the symbiotic relationship between IR telescopic observations and laboratory work has continually revealed that these ices host a rich solid-state chemistry that is foundational to the formation and transport of volatiles during the formation of planetary systems. However, a number of pressing questions about this chemistry also remained unanswered when this thesis work began:

- **To what extent is interstellar ice inherited versus chemically reprocessed in protostellar envelopes and protoplanetary disks before its accretion into planetary objects?** Comparisons of volatile abundances between interstellar ices and primitive solar system objects like comets show both striking similarities as well as key differences, suggesting that interstellar ices play an important role in setting planetary compositions but do also experience some level of chemical alteration throughout the star formation process (see Section 1.2.3). At what points during this process are interstellar ices preserved, and at what points are they reprocessed? *(addressed in Chapters 1 & 2)*

- **What species are the major sulfur sinks in the densest stages of star formation?** Sulfur is a key biogenic element, and its elemental abundance observed in the interstellar medium (Esteban et al. 2004) is close to the abundance observed in the sun and in primitive meteorites (Lodders 2003; Asplund et al. 2009). However, the sulfur abundance observed in the most dense stages of star formation (*e.g.*, molecular clouds and protostellar envelopes) can be up to 2-3 orders of magnitude lower than these interstellar and solar values. Models have long suggested much of the sulfur is expected to freeze out on the dust grains and form S-bearing ices, particularly H_2S (*e.g.*, Garrod et al. 2007), yet measured abundances of S-ices in these dense environments remain too low to account for the missing sulfur. In what chemical form is sulfur hiding in dense interstellar regions? And why are upper limits of species like H_2S so low despite model predictions? *(addressed in Chapters 3 & 4)*

- **Which of the many complex organic molecules detected in the gas phase in protostars can be found also in ices, and what does that tell us about their formation histories?** Despite the hundreds of chemically unique molecules detected in star-forming regions, very few molecules have been securely detected in interstellar ices – the so-called *gas-grain* gap. Some of the species detected in the gas phase may not be detected in ices because the species are produced via gas phase chemical routes, but others may not have been detected yet due to observational limitations or a lack of the necessary laboratory data. By how much will the combination of new facilities with improved sensitivity and spectral resolution like JWST and growing databases of laboratory data close this gap? *(addressed in Chapter 6)*

1.4.2 Chapter summary

Water ice D/H ratios as a probe of ice inheritance

Chapter 2: This work uses the increased sensitivity and resolution of JWST to make the first robust detections of the O-D stretching mode of HDO ice at 4.1 μm. It then presents a method for quantifying ice HDO/H_2O ratios toward protostellar lines of sight with thermal gradients and uses this method to find this ratio toward two massive protostars observed with JWST. For this work, new laboratory IR spectra of ice mixtures containing HDO, H_2O, CH_3OH, and CO were collected to aid in the fitting and chemical interpretation of the observed spectra. HDO ice is detected above the 3σ level toward both sources, with fits requiring a combination of HDO in mixtures with amorphous and crystalline H_2O. Ice HDO/H_2O ratios of $4.6\pm1.8\times10^{-3}$ and $2.6\pm1.2\times10^{-3}$ are obtained for the two sources. These ratios are similar to the highest reported gas HDO/H_2O ratios measured toward massive protostars and the hot inner regions of isolated low-mass protostars, suggesting that at least some of the gas HDO/H_2O ratios measured toward massive hot cores are representative of those in ices.

Chapter 3: This work presents the first detection of the 4.1 μm HDO ice feature with JWST toward a low-mass protostar, L1527 IRS, which may eventually grow to a Sun-like mass The method developed in Chapter 2 is used to measure an ice HDO/H_2O ratio of $4.4^{+3.7}_{-1.7}\times10^{-3}$, similar to the gas HDO/H_2O ratios measured in the warm inner cores of other low-mass protostellar envelopes and protoplanetary disks found in comparably isolated star-forming regions. Such a similarity tentatively supports the assumption that water vapor detected in these regions is not significantly altered by gas-phase reactions following ice sublimation. It also supports the hypothesis that pre- and protostellar water ice is largely inherited in a chemically unaltered state by outer protoplanetary disks. However, the fraction is a factor of $\sim$4-10 times higher than the gas HDO/H_2O ratios measured toward comets and low-mass protostars in clustered star-forming regions. This difference may be due to either gas-phase water reprocessing in protostellar envelopes and protoplanetary disks or differences between prestellar conditions of isolated dense cores and the clustered star-forming regions that are more analogous to the environment in which our Sun formed.

Sulfur ice chemistry

Chapter 4: Laboratory transmission IR spectra of both pure and H_2O-rich ices containing NH_4SH salt were collected to spectroscopically investigate the plausibility of NH_4SH serving as a sulfur reservoir and a carrier of the 6.85 μm band in interstellar ices. Peak positions, full width half maxima, and apparent band strengths of the NH_4^+ asymmetric bending mode and the SH^- stretching mode in H_2O-rich ices were obtained. The IR features of the laboratory salts were compared to those observed toward a sample of four protostars and two cold dense clouds. The observed 6.85 μm feature toward these sources is fit well with the laboratory NH_4SH:H_2O ice spectra, and the fits provide NH_4^+ column densities that range from 8–23% with respect to H_2O. Furthermore, the redshift of the 6.85 μm feature correlates with higher abundances of NH_4^+ with respect to H_2O in both the laboratory and observational data. The apparent band strength of the SH^- feature is likely too low for the feature to be detectable, but the 5.3 μm $NH_4^+ + SH^-$ combination mode may be an alternative means of detection. Its tentative assignment adds to mounting evidence supporting the presence of NH_4^+ salts in ices and is the first tentative observation of the SH^- anion toward interstellar ices. The combined

upper limits of four other counter-anion candidates, OCN^-, CN^-, $HCOO^-$, and Cl^-, are determined to be $\lesssim$15–20% of the total NH_4^+ column densities toward three of the protostars. If the majority ($\gtrsim$80–85%) of the NH_4^+ cations quantified toward the investigated sources in this work are bound to SH^- anions, then NH_4SH salts could account for up to 17–18% of their sulfur budgets.

Chapter 5: This chapter provides a library of new laboratory IR transmission spectra of OCS in CH_3OH- and CO-rich ice mixtures, some of which also include H_2S and H_2O, to aid future studies of the abundance, physicochemical environment, and evolutionary history of interstellar OCS ice. Of these new laboratory spectra, the tertiary OCS:CO:CH_3OH ice mixtures provide the best fits to observations of high-mass protostars, providing further support for the hypothesis that OCS forms with CH_3OH, possibly via chemical pathways involving frozen-out CO. The apparent band strengths of the ν_3 mode in OCS:CH_3OH and OCS:CO:CH_3OH ice mixtures are calculated. The derived values are consistent (within uncertainties) with the apparent band strength of the feature in pure OCS ice. A calibration method for producing ice mixtures using gases and high vapor pressure liquids is described.

Hunt for complex organic molecules in ices

Chapter 6: Gaseous formamide has been detected in many interstellar regions, but whether it forms in the ice or gas is a topic of great debate. However, more laboratory data are needed to hunt for its presence in interstellar ices. This chapter characterizes the IR spectra of formamide in its pure form as well as in mixtures of the most abundant interstellar ices. Apparent band strengths and positions of eight IR bands of formamide at various temperatures are provided. Three of these bands are identified as potential formamide tracers in observational ice spectra: the overlapping C=O stretch and NH_2 scissor bands at 5.88 and 6.13 μm, the CH bend at 7.20 μm, and the CN stretch at 7.53 μm. The laboratory spectra are compared to observational spectra of low- and high-mass protostars as well as prestellar cores. A comparison between the formamide CH bend in laboratory data and the 7.24 μm band in the observations tentatively indicates that, if formamide ice is contributing significantly to the observed absorption, it is more likely in a polar matrix, but other species like $HCOO^-$ and CH_3CH_2OH provide better fits to this feature and are more likely to be the main carriers of this band. Upper limits ranging from 0.35-5.1% with respect to H_2O were calculated. These upper limits are in agreement with gas-phase protostellar as well as cometary formamide abundances.

1.4.3 Scientific significance and future directions

The key scientific takeaways of this thesis can be summarized as follows:

- HDO ice is now robustly detectable in star-forming regions with JWST. Similarities between ice and gas water D/H ratios measured toward protostars and the gas water D/H measured toward protoplanetary disks suggest interstellar ice inheritance between protostellar envelopes and protoplanetary disks.

- Comparisons between water D/H values in protostellar ices and cometary comae suggest either some level of gas-phase water reprocessing in the protoplanetary disk *or* or

an environmentally-driven diversity in prestellar water ice D/H values across different star-forming regions in our galaxy.

- Up to ∼20% of the sulfur in dense star-forming regions like molecular clouds and protostellar envelopes may be locked up in salts like NH_4SH, potentially resolving the decades-long puzzle of why H_2S is not detected in interstellar ices despite predictions from chemical models.
- Given their higher desorption temperatures relative to their neutral acid-base counterparts, salts like NH_4SH may have facilitated the transport of the volatile elements N and S into the inner solar system, where they could eventually be accreted by volatile-rich bodies like carbonaceous asteroids.[2]
- Even with JWST, it may not be possible to unambiguously detect the absorption features of many of the less abundant and semi-refractory complex organic molecules like formamide due to overlaps with absorptions from more abundant and volatile organics.

Looking forward, a larger sample of ice water D/H measured toward protostars spanning a variety of environments will be needed to better constrain the ice water D/H ratio that was likely inherited by our solar system. Furthermore, a large fraction of the interstellar sulfur still remains missing. If it is in minerals or allotropes as suggested by others (Jiménez-Escobar & Caro 2011; Shingledecker et al. 2020), chances for direct detections of such species are not promising. But wherever this missing sulfur may be, it is time for an updated sulfur ice survey with JWST data to update previous constraints on species like H_2S and OCS, which primarily used outdated band strengths and focused on high-mass systems. The laboratory data presented in this thesis enable such surveys. And finally, observationally targeting lines of sight with low volatile ice-to-dust ratios but high dust columns (*i.e.*, protostellar envelopes that are still dense but have beeen highly thermally or energetically processed) may provide better opportunities for identifying more refractory trace ice species whose absorptions are typically overshadowed by the strong absorptions of the more abundant volatiles.

[2]For example, the liquid H_2O:NH_3 inclusions within iron sulfide grains found in recently returned samples from the carbonaceous asteroid Bennu may be a result of the aqueous alteration of this salt within Bennu's parent body (Prince et al. 2025).

1.B Bibliography

Alexander, C. M. 2017, Phil. Trans. R. Soc. A, Math. Phys. Eng. Sci., 375
Alexander, C. O., Fogel, M., Yabuta, H., & Cody, G. 2007, GCA, 71, 4380
Allodi, M., Baragiola, R., Baratta, G., et al. 2013, SSRv, 180, 101
Altwegg, K., Combi, M., Fuselier, S., et al. 2022, MNRAS, 516, 3900
Arumainayagam, C. R., Garrod, R. T., Boyer, M. C., et al. 2019, Chem. Soc. Rev., 48, 2293
Asplund, M., Grevesse, N., Sauval, A. J., & Scott, P. 2009, ARA&A, 47, 481
Baratta, G. & Palumbo, M. 1998, J. Opt. Soc. Am. A, 15, 3076
Bergner, J. B., Sturm, J., Piacentino, E. L., et al. 2024, ApJ, 975, 166
Bernstein, M. P., Dworkin, J. P., Sandford, S. A., Cooper, G. W., & Allamandola, L. J. 2002, Nature, 416, 401
Beuther, H., Churchwell, E. B., McKee, C. F., & Tan, J. C. 2007, Protostars and Planets V, 165
Beuther, H., Kuiper, R., & Tafalla, M. 2025, ARA&A, 63
Boogert, A., Brewer, K., Brittain, A., & Emerson, K. 2022, ApJ, 941, 32
Boogert, A., Chiar, J., Knez, C., et al. 2013, ApJ, 777, 73
Boogert, A., Ehrenfreund, P., Gerakines, P., et al. 2000, A&A, 353, 349
Boogert, A. A., Gerakines, P. A., & Whittet, D. C. 2015, ARA&A, 53, 541
Boogert, A. C., Pontoppidan, K. M., Knez, C., et al. 2008, ApJ, 678, 985
Bottinelli, S., Boogert, A. A., Bouwman, J., et al. 2010, ApJ, 718, 1100
Brown, W. A. & Bolina, A. S. 2007, MNRAS, 374, 1006
Brunken, N., van Dishoeck, E., Slavicinska, K., et al. 2024a, A&A, 692, A163
Brunken, N. G., Rocha, W. R., van Dishoeck, E. F., et al. 2024b, A&A, 685, A27
Busch, L. A., Belloche, A., Garrod, R. T., Müller, H. S., & Menten, K. M. 2022, A&A, 665, A96
Chen, Y., Rocha, W. R. M., van Dishoeck, E. F., et al. 2024, A&A, 690, A205
Chuang, K.-J., Fedoseev, G., Ioppolo, S., van Dishoeck, E., & Linnartz, H. 2016, MNRAS, 455, 1702
Chuang, K.-J., Jäger, C., Krasnokutski, S., Fulvio, D., & Henning, T. 2022, ApJ, 933, 107
Cleeves, L. I., Bergin, E. A., Alexander, C. M. O., et al. 2014, Science, 345, 1590
Collings, M. P., Anderson, M. A., Chen, R., et al. 2004, MNRAS, 354, 1133
Corliss, J. B., Baross, J., & Hoffman, S. 1981, Oceanol. Acta, 59
Cuppen, H., Penteado, E., Isokoski, K., van der Marel, N., & Linnartz, H. 2011, MNRAS, 417, 2809
Cuppen, H. M., Linnartz, H., & Ioppolo, S. 2024, ARA&A, 62
Dartois, E. & d'Hendecourt, L. 2001, A&A, 365, 144
Dartois, E., Noble, J. A., Caselli, P., et al. 2024, Nat. Astro., 8, 359
Dartois, E., Noble, J. A., Ysard, N., Demyk, K., & Chabot, M. 2022, A&A, 666, A153
Di Giulio, M. 2003, J. Theor. Biol., 221, 425
Draine, B. T. 1978, ApJS, 36, 595
Drozdovskaya, M. N., van Dishoeck, E. F., Rubin, M., Jørgensen, J. K., & Altwegg, K. 2019, MNRAS, 490, 50
Drozdovskaya, M. N., Walsh, C., Visser, R., Harsono, D., & van Dishoeck, E. F. 2014, MNRAS, 445, 913
Dunham, M. M., Stutz, A. M., Allen, L. E., et al. 2014, Protostars and Planets VI, 195

Ehrenfreund, P., Boogert, A., Gerakines, P., Tielens, A., & van Dishoeck, E. 1997, A&A, 328, 649
Ehrenfreund, P., Dartois, E., Demyk, K., & d'Hendecourt, L. 1998, A&A, 339, L17
Ehrenfreund, P. & van Dishoeck, E. 1998, Adv. Space Res., 21, 15
Esteban, C., Peimbert, M., García-Rojas, J., et al. 2004, MNRAS, 355, 229
Fedoseev, G., Chuang, K.-J., Ioppolo, S., et al. 2017, ApJ, 842, 52
Fedoseev, G., Ioppolo, S., Zhao, D., Lamberts, T., & Linnartz, H. 2015, MNRAS, 446, 439
Frenkel-Pinter, M., Rajaei, V., Glass, J. B., Hud, N. V., & Williams, L. D. 2021, J. Mol. Evol., 89, 2
Garrod, R. T. & Herbst, E. 2006, A&A, 457, 927
Garrod, R. T., Wakelam, V., & Herbst, E. 2007, A&A, 467, 1103
Garrod, R. T., Weaver, S. L. W., & Herbst, E. 2008, ApJ, 682, 283
Gerakines, P. A. & Hudson, R. L. 2020, ApJ, 901, 52
Gibb, E., Whittet, D., Boogert, A., & Tielens, A. 2004, ApJS, 151, 35
Gillett, F. & Forrest, W. 1973, ApJ, 179, 483
Hiraoka, K., Ohashi, N., Kihara, Y., et al. 1994, Chem. Phys. Lett., 229, 408
Hiraoka, K., Yamashita, A., Yachi, Y., et al. 1995, ApJ, 443, 363
Hollenbach, D. & Salpeter, E. 1971, ApJ, 163, 155
Hubbard, G. S., Naderi, F. M., & Garvin, J. B. 2002, Acta Astronaut., 51, 337
Jensen, S., Jørgensen, J., Kristensen, L., et al. 2019, A&A, 631, A25
Jiménez-Escobar, A. & Caro, G. M. 2011, A&A, 536, A91
Kaifu, N., Ohishi, M., Kawaguchi, K., et al. 2004, PASJ, 56, 69
Kaňuchová, Z., Urso, R., Baratta, G., et al. 2016, A&A, 585, A155
Klessen, R. S. & Glover, S. C. 2015, in Star Formation in Galaxy Evolution: Connecting Numerical Models to Reality: Saas-Fee Advanced Course 43. Swiss Society for Astrophysics and Astronomy (Springer), 85–249
Ligterink, N., Paardekooper, D., Chuang, K.-J., et al. 2015, A&A, 584, A56
Lodders, K. 2003, ApJ, 591, 1220
Mandt, K. E., Lustig-Yaeger, J., Luspay-Kuti, A., et al. 2024, Sci. Adv., 10, eadp2191
Martin, W., Baross, J., Kelley, D., & Russell, M. J. 2008, Nat. Rev. Microbiol., 6, 805
Mastrapa, R., Sandford, S., Roush, T., Cruikshank, D., & Dalle Ore, C. 2009, ApJ, 701, 1347
McClure, M. K., Rocha, W., Pontoppidan, K., et al. 2023, Nat. Astro., 7, 431
McGuire, B. A. 2022, ApJS, 259, 30
Moody, E. R., Álvarez-Carretero, S., Mahendrarajah, T. A., et al. 2024, Nat. Ecol. Evol., 8, 1654
Mumma, M. J. & Charnley, S. B. 2011, ARA&A, 49, 471
Munoz Caro, G., Meierhenrich, U. J., Schutte, W. A., et al. 2002, Nature, 416, 403
Nazari, P., Rocha, W., Rubinstein, A., et al. 2024, A&A, 686, A71
Noble, J. A., Fraser, H., Smith, Z., et al. 2024, Nat. Astro., 8, 1169
Novozamsky, J., Schutte, W., & Keane, J. 2001, A&A, 379, 588
Oba, Y., Takano, Y., Naraoka, H., Watanabe, N., & Kouchi, A. 2019, Nat. Comm., 10, 4413
Oba, Y., Watanabe, N., Kouchi, A., Hama, T., & Pirronello, V. 2010, ApJL, 712, L174
Öberg, K. I. 2016, Chem. Rev., 116, 9631
Öberg, K. I. & Bergin, E. A. 2021, Phys. Rep., 893, 1
Öberg, K. I., Boogert, A. A., Pontoppidan, K. M., et al. 2008, ApJ, 678, 1032
Öberg, K. I., Boogert, A. A., Pontoppidan, K. M., et al. 2011, ApJ, 740, 109

Omont, A., Moseley, S., Forveille, T., et al. 1990, ApJL, 355, L27
Ootsubo, T., Kawakita, H., Hamada, S., et al. 2012, ApJ, 752, 15
Pace, N. R. 1991, Cell, 65, 531
Paganini, L., Mumma, M., Gibb, E., & Villanueva, G. L. 2017, ApJL, 836, L25
Palumbo, M., Geballe, T., & Tielens, A. G. 1997, ApJ, 479, 839
Palumbo, M. E., Baratta, G. A., Collings, M. P., & McCoustra, M. R. 2006, PCCP, 8, 279
Persson, M., Jørgensen, J., van Dishoeck, E., & Harsono, D. 2014, A&A, 563, A74
Pineda, J. E., Segura-Cox, D., Caselli, P., et al. 2020, Nat. Astro., 4, 1158
Poch, O., Istiqomah, I., Quirico, E., et al. 2020, Science, 367, eaaw7462
Pontoppidan, K., Fraser, H., Dartois, E., et al. 2003, A&A, 408, 981
Pontoppidan, K. M. 2006, A&A, 453, L47
Pontoppidan, K. M., Boogert, A. C., Fraser, H. J., et al. 2008, ApJ, 678, 1005
Prasad, S. S. & Tarafdar, S. P. 1983, ApJ, 267, 603
Prince, B. S., Gainsforth, Z., Benner, M. C., & Zega, T. J. 2025, Microsc. Microanal., 31, 1447
Qasim, D., Chuang, K.-J., Fedoseev, G., et al. 2018, A&A, 612, A83
Qasim, D., Fedoseev, G., Chuang, K.-J., et al. 2020, Nat. Astro., 4, 781
Qasim, D., Fedoseev, G., Chuang, K.-J., et al. 2019, A&A, 627, A1
Rachid, M., Brunken, N., De Boe, D., et al. 2021, A&A, 653, A116
Robitaille, T. P., Whitney, B. A., Indebetouw, R., Wood, K., & Denzmore, P. 2006, ApJS, 167, 256
Rocha, W., van Dishoeck, E., Ressler, M., et al. 2024, A&A, 683, A124
Russell, M., Hall, A., Cairns-Smith, A., & Braterman, P. 1988, Nature, 336, 117
Russell, M. J. & Martin, W. 2004, Trends Biochem. Sci., 29, 358
Santos, J. C., Linnartz, H., & Chuang, K.-J. 2024, A&A, 690, A24
Segura-Cox, D. M., Schmiedeke, A., Pineda, J. E., et al. 2020, Nature, 586, 228
Shen, C., Greenberg, J., Schutte, W., & van Dishoeck, E. 2004, A&A, 415, 203
Shingledecker, C. N., Lamberts, T., Laas, J. C., et al. 2020, ApJ, 888, 52
Smith, D. 1992, Chem. Rev., 92, 1473
Smith, R. G., Sellgren, K., & Tokunaga, A. T. 1989, ApJ, 344, 413
Stevenson, D. J. & Lunine, J. I. 1988, Icarus, 75, 146
Sturm, J., McClure, M., Beck, T., et al. 2023, A&A, 679, A138
Terwisscha van Scheltinga, J., Ligterink, N., Boogert, A., van Dishoeck, E., & Linnartz, H. 2018, A&A, 611
Tielens, A. & Hagen, W. 1982, A&A, 114, 245
Tyagi, H., Manoj, P., Narang, M., et al. 2025, ApJ, 983, 110
Valdivia-Mena, M. T., Pineda, J. E., Caselli, P., et al. 2024, A&A, 687, A71
van Broekhuizen, F., Keane, J., & Schutte, W. 2004, A&A, 415, 425
van Dishoeck, E. 1992, in Symposium-International Astronomical Union, Vol. 150, Cambridge University Press, 143–151
van Dishoeck, E. F. & Black, J. H. 1988, ApJ, 334, 771
van Dishoeck, E. F., Kristensen, L. E., Mottram, J. C., et al. 2021, A&A, 648, A24
van Dishoeck, E. F., Tychoniec, Ł., Rocha, W. R. M., et al. 2025, A&A, 699, A361
Vidali, G. 2013, Chem. Rev., 113, 8762
Viti, S. & Williams, D. A. 1999, MNRAS, 305, 755
Wakelam, V., Bron, E., Cazaux, S., et al. 2017, Mol. Astrophys., 9, 1

Watanabe, N. & Kouchi, A. 2002, ApJ, 571, L173
Weiss, M. C., Sousa, F. L., Mrnjavac, N., et al. 2016, Nat. Microbiol., 1, 1
Whittet, D., Poteet, C., Chiar, J., et al. 2013, ApJ, 774, 102
Whittet, D., Shenoy, S., Bergin, E., et al. 2007, ApJ, 655, 332
Williams, J., Krijt, S., Bitsch, B., Houge, A., & Bergner, J. 2025, MNRAS, 544, 3562
Yang, L., Ciesla, F. J., & Alexander, C. M. 2013, Icarus, 226, 256
Yarnall, Y. Y. & Hudson, R. L. 2022, ApJL, 931, L4
Zolensky, M. E., Zega, T. J., Yano, H., et al. 2006, Science, 314, 1735